LA-UR -85-4448

CONF-8208336--3

Los Alamos National Laboratory is operated by the University of California for the United States Department of Energy under contract W-7405-ENG-36

LA-UR--85-4448

DE86 004749

TITLE: 2-D EULERIAN HYDRODYNAMICS WITH FLUID INTERFACES, SELF-GRAVITY AND ROTATION

AUTHOR(S). Michael L. Norman and Karl-Heinz A. Winkler

SUBMITTED TO Astrophysical Radiation Hydrodynamics
Proceedings of NATO Advanced Research Workshop
Garching, W. Germany, August 2-13, 1982.

DISCLAIMER

Los Alamos Los Alamos National Laboratory
Los Alamos, New Mexico 87545

2-D EULERIAN HYDRODYNAMICS WITH FLUID INTERFACES, SELF-GRAVITY AND ROTATION

Michael L. Norman and Karl-Heinz A. Winkler

Los Alamos National Laboratory and
Max-Planck-Institut für Physik und Astrophysik

1. INTRODUCTION

The purpose of this paper is to describe in detail the numerical approach we have developed over the past five years for solving 2-dimensional gas-dynamical problems in astrophysics involving inviscid compressible flow, self-gravitation, rotation, and fluid instabilities of the Rayleigh-Taylor and Kelvin-Helmholtz types. The computer code to be described has been applied most recently to modeling jets in radio galaxies (Norman et al. 1981, 1982) and is an outgrowth of a code developed for studying rotating protostellar collapse (Norman, Wilson and Barton 1980; Norman 1980). The basic methodology draws heavily on the techniques and experience of James R. Wilson and James M. LeBlanc of the Lawrence Livermore National Laboratory, and thus the code is designed to be a general purpose 2-D Eulerian hydrocode, and is characterized by a high degree of simplicity, robustness, modularity and speed. Particular emphases of this article are: 1) the recent improvements to the code's accuracy through the use of vanLeer's (1977) monotonic advection algorithm, 2) a discussion of the importance of what we term consistent advection, and 3) a description of a numerical technique for modeling dynamic fluid interfaces in multidimensional Eulerian calculations developed by LeBlanc.

The outline of this paper is as follows. In Sec. 2 we present the physical equations and our two-step methodology for solving them. Finite-difference equations for these two steps -the source step and transport step- are given in Secs. 3 and 4, respectively. The fluid interface technique we use is then described and discussed in Sec. 5. In Sec. 6 we summarize our iterative alternating-direction-implicit (ADI) procedure for solving the Poisson equation. Our timestep control procedure is given in Sec. 7. Finally, Sec. 8 contains several applications of this code to astrophysical problems of current interest involving fluid interfaces, self-gravity and rotation.

2. BASIC EQUATIONS AND METHODOLOGY

2.1 Fluid Equations in moving coordinates

In applications involving gravitational collapse or explosions, a moving coordinate mesh is used to maintain adequate problem coverage and zoning resolution. We therefore begin by writing the basic equations of self-gravitating ideal gas dynamics in such a coordinate system:

continuity equation

$$d/dt \int \rho d\tau + \int \rho(v-v_g)\cdot d\Sigma = 0, \qquad (1)$$

momentum equation

$$d/dt \int \rho v d\tau + \int \rho v(v-v_g)\cdot d\Sigma + \int (\nabla P + \rho\nabla\Phi)d\tau = 0, \qquad (2)$$

internal energy equation

$$d/dt \int \rho\varepsilon d\tau + \int \rho\varepsilon(v-v_g)\cdot d\Sigma + \int P\nabla\cdot v d\tau = 0. \qquad (3)$$

Here, the time derivatives and spatial integrations operate on the moving grid zone of volume $d\tau$ and surface area $d\Sigma$ moving with velocity v_g with respect to a fixed (Eulerian) observer; ρ, ε and v are the fluid's mass density, specific internal energy and Eulerian velocity, respectively. The pressure P will usually be computed from the ideal gas law $P=(\gamma-1)\rho\varepsilon$, where γ is the ratio of specific heats, although introducing a general equation of state $P=P(\rho,\varepsilon)$ offers no principle difficulties. The gravitational potential Φ is computed from the Poisson equation

$$\nabla^2\Phi = 4\pi G\rho. \qquad (4)$$

Equations (1)-(4) form a complete set once v_g is specified, and are sufficient to determine the problem for given initial and boundary conditions. Note that if one sets $v_g=0$ in eqs. (1)-(3), then d/dt becomes the Eulerian time derivative $\partial/\partial t$, which commutes with the volume integral. Applying the divergence theorem, one easily recovers the Eulerian differential equations of hydrodynamics.

2.2 Two-step solution procedure

Explicit multi-step solution procedures for solving the equations of hydrodynamics are generally more accurate than a single step that simply extrapolates forward in time on the basis of old data. Before we specialize eqs. (1)-(4) to a particular geometry and begin writing down difference equations, we would like to describe our two-step approach to solving the fluid equations which is independent of geometry or dimensionality.

Eqs. (1)-(3) are solved in two logically independent steps which we call the *source* and *transport* steps. In the source step, we accelerate fluid velocities and perform pressure work on the gas internal energy by solving finite-difference approximations to the following differential equations:

$$\rho dv/dt = -(\nabla P + \rho\nabla\Phi) - \nabla\cdot Q \tag{5}$$

$$\rho d\varepsilon/dt = -P\nabla\cdot v - Q:\nabla v\,, \tag{6}$$

We have introduced additional terms involving Q in eqs. (5) and (6), which represent acceleration and heating due to artificial viscous stresses used to mediate the numerical shock transitions. In the transport step, fluid is transported through the computational mesh by solving finite-difference approximations to the following integral equations:

$$d/dt \int \rho\, d\tau = -\int \rho\,(v-v_g)\cdot d\Sigma, \tag{7}$$

$$d/dt \int \rho v d\tau = -\int \rho v (v-v_g)\cdot d\Sigma, \tag{8}$$

$$d/dt \int \rho\varepsilon d\tau = -\int \rho\varepsilon (v-v_g)\cdot d\Sigma. \tag{9}$$

The updated values of v and ε from the source steps are used to evaluate the right-hand-sides of eqs. (7)-(9), and enter as the old values in the time-discretized left-hand-sides of eqs. (8) and (9).

To understand the origin of these equations, consider the momentum equation in differential form, whicl. can be derived from eq. (2) using the identity

$$\nabla\cdot v_g \equiv d/dt\ (\ln d\tau). \tag{10}$$

Letting $S = \rho v$, we have

$$dS/dt + S\nabla\cdot v_g + \nabla\cdot[(v-v_g)S] + \nabla P + \nabla\cdot Q + \rho\nabla\Phi = 0 \tag{11}$$

which we solve incrementally as

$$dS/dt = dS/dt)_{source} + dS/dt)_{transport} \tag{12}$$

where

$$dS/dt)_{source} = -(\nabla P + \rho\nabla\Phi) - \nabla\cdot Q, \tag{13}$$

and

$$dS/dt)_{transport} = -\nabla\cdot[(v-v_g)S] - S\nabla\cdot v_g. \tag{14}$$

Noting $d\rho/dt)_{source} = 0$ in eq. (13), we recover eq. (5); integrating eq. (14) over a moving volume we recover eq. (8) using eq. (10). The advantage of the integral formulation for the transport step is that it is in conservative form in a moving coordinate system, whereas eq. (14) is not due to the grid compression term. Moreover, an integral formulation is manditory for advecting fluid interfaces, which, since we treat them numerically as true discontinuities, cannot be described by differential equations.

3. SOURCE STEP

3.1 Grid and variables

Let U, V and W be the velocity components of a fluid element in the Z, R and θ directions, respectively, of a cylindrical coordinate system, and let $S=\rho U$, $T=\rho V$, and $A=\rho \sqrt{R} \equiv \rho \Omega R^2$ be the element's associated linear momentum density components and angular momentum density, respectively. Then, using the fact that $d\rho/dt)_{source} = 0$, we write eq. (5) in the explicit component form in which it is differenced as

$$dS/dt)_{source} = - \partial P/\partial Z - \rho \partial \Phi/\partial Z - \partial Q^{ZZ}/\partial Z, \quad (15)$$

$$dT/dt)_{source} = - \partial P/\partial R - \rho \partial \Phi/\partial R - \partial Q^{RR}/\partial R + \rho \Omega^2 R. \quad (16)$$

$$dA/dt)_{source} = 0, \quad (17)$$

and write eq. (6) as

$$dE/dt)_{source} = - P(\partial U/\partial Z + R^{-1} \partial RV/\partial R) - Q^{ZZ} \partial U/\partial Z - Q^{RR} \partial V/\partial R, \quad (18)$$

where $E=\rho\varepsilon$ is the internal energy density. Notice that only the diagonal elements of the artificial viscosity tensor have been retained in eqs. (15, 16 and 18), and that geometric terms such as Q^{RR}/R and $Q^{RR}V/R$ have not been included. The reasons for this are, first, we want artificial viscosity to be sensitive only to compressions to pick out shock fronts, hence we discard the off-diagonal elements, and second, we want the numerical shock width to be the same regardless of its distance from the symmetry axis, as it would be in nature on a macroscopic scale. Note, however, that a proper tensor formulation may be required for the artificial viscosity if special properties are sought (see Winkler and Norman, this volume).

The centering of the variables on the finite difference mesh and zone measurements are shown in Fig. 1. The Z and R grid lines have indices k and j respectively. Linear momentum and velocity components are located at the zone faces; scalar densities, the gravitational potential and the angular momentum density are located at the zone center. The velocity components U and V are derived by dividing their respective momentum components by an arithmetic average of the two adjacent mass densities.

3.2 Difference equations

The location of the quantities on the mesh (Fig. 1) allow for simple centered differences and averages of the terms appearing on the right-hand-sides of eqs. (15,16 and 18). These equations are solved in steps as follows: 1) accelerate S and T due to pressure, gravitational and centrifugal forces; 2) using the updated velocities, compute the artificial viscous heating and acceleration; 3) using the updated E and velocity components from step 2), perform compressional heating on the gas. Thus, letting the superscripts a, q and p represent the updated values from the three steps and the unsuperscripted quantities represent values at the old

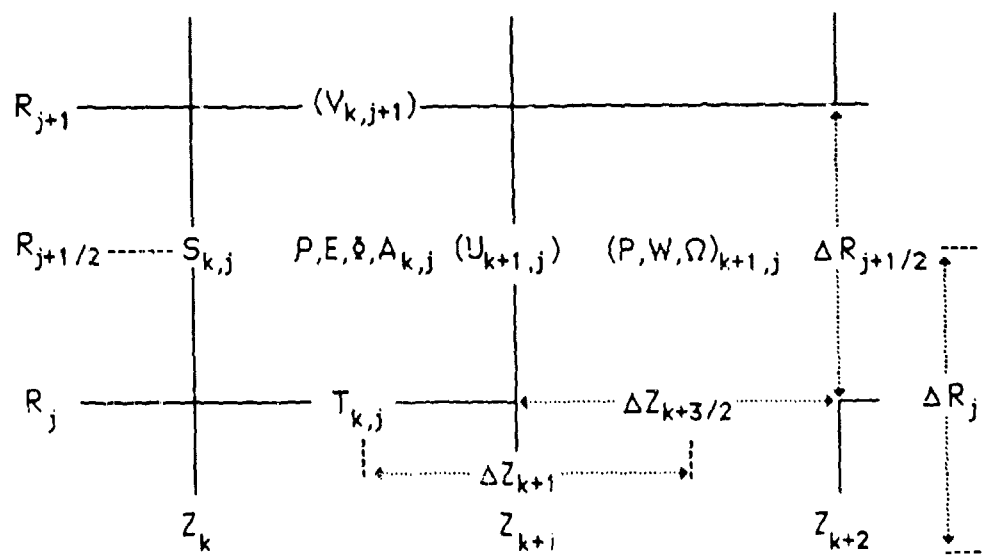

Fig. 1 Centering of the primary and secondary (derived) quantities on the mesh (Z_k,R_j).

time level, we solve the following explicit difference equations:

<u>step 1</u>

$$(S^a\text{-}S)_{k,j} / \delta t = -[(P_{k,j}-P_{k-1,j}) + \langle\rho\rangle_Z(\Phi_{k,j}-\Phi_{k-1,j})] / \Delta Z_k, \tag{19}$$

$$(T^a\text{-}T)_{k,j} / \delta t = -[(P_{k,j}-P_{k,j-1}) + \langle\rho\rangle_R(\Phi_{k,j}-\Phi_{k,j-1})] / \Delta R_j + \langle\rho\rangle_R \langle\Omega\rangle_R{}^2 R_j, \tag{20}$$

where the spatial averages are defined $\langle X\rangle_Z = (X_{k,j}+X_{k-1,j})/2$ and $\langle X\rangle_R = (X_{k,j}+X_{k,j-1})/2$. The form of the centrifugal force term may vary according to application; averaging on Ω as opposed to W, say, is superior when $\Omega(R)$=constant.

<u>step 2</u>

$$(S^q\text{-}S^a)_{k,j} / \delta t = -(Q^{ZZ}{}_{k,j}-Q^{ZZ}{}_{k-1,j})/\Delta Z_k, \tag{21}$$

$$(T^q\text{-}T^a)_{k,j} / \delta t = -(Q^{RR}{}_{k,j}-Q^{RR}{}_{k,j-1})/\Delta R_j, \tag{22}$$

$$(E^q-E)_{k,j}/\delta t = -Q^{ZZ}_{k,j}(U^a_{k+1,j}-U^a_{k,j})/\Delta Z_{k+1/2} - Q^{RR}_{k,j}(V^a_{k,j+1}-V^a_{k,j})/\Delta R_{j+1/2}, \quad (23)$$

where

$$Q^{ZZ}_{k,j} = \rho_{k,j}(U^a_{k+1,j}-U^a_{k,j})[-C_1 a + C_2 \min(U^a_{k+1,j}-U^a_{k,j},0)], \quad (24)$$

$$Q^{RR}_{k,j} = \rho_{k,j}(V^a_{k,j+1}-V^a_{k,j})[-C_1 a + C_2 \min(V^a_{k,j+1}-V^a_{k,j},0)]. \quad (25)$$

Here C_1 and C_2 are constants of order unity which govern the linear and quadratic artificial viscosities and a is the adiabatic speed of sound. The linear viscosity is rarely used, and then only sparingly to damp oscillations in stagnant regions of the flow.

step 3

Here, to improve energy conservation, we write an implicit difference equation involving the time-centered pressure $P^{n+1/2}=[P^n+(\gamma-1)E^p]/2$ in $P\nabla\cdot v$ which can be rearranged and solved explicitly:

$$(E^p-E^q)_{k,j}/\delta t = -[P^n+(\gamma-1)E^p]/2\,(\nabla\cdot v)_{k,j}, \quad (26)$$

or

$$E^p_{k,j} = [E^q-P^n\delta t(\nabla\cdot v)/2]_{k,j} / [1+(\gamma-1)\delta t(\nabla\cdot v)/2]_{k,j}, \quad (27)$$

where

$$(\nabla\cdot v)_{k,j} = (U^q_{k+1,j}-U^q_{k,j})/\Delta Z_{k+1/2} + (R_{j+1}V^q_{k,j+1}-R_j V^q_{k,j})/(R_{j+1/2}\Delta R_{j+1/2}). \quad (28)$$

This procedure explicitly assumes a gamma-law gas; for a general equation of state $P=P(\rho,\varepsilon)$, we use a predictor-corrector approach to find the time-centered pressure, thus

predictor step

$$(E'-E^q)_{k,j}/\delta t = -P^n(\nabla\cdot v)_{k,j}, \quad (29)$$

corrector step

$$(E^p-E^q)_{k,j}/\delta t = -[P^n+P']/2(\nabla\cdot v)_{k,j}, \quad (30)$$

where

$$P' = P(\rho,E'/\rho)\,. \quad (31)$$

Experience has shown that energy conservation is improved by using the same

pressure in eqs. (19-21) as is used for acceleration (i.e., P^n rather than, say $(\gamma-1)E^q$.)

4. TRANSPORT STEP

We now describe our numerical procedure for solving eqs. (7-9), which are all of the form

$$d/dt \int q\, d\tau = -\int q\,(v-v_g)\cdot d\Sigma. \tag{32}$$

Equation (32) is manifestly in conservative form, and describes the advection of a quantity q on the moving mesh allowing for volumetric changes due to fluid (v) and zonal (v_g) convergence. This compound process we term *transport*. The obvious second-order accurate finite-difference approximation to eq. (32) is

$$(q^{n+1}\tau^{n+1}-q^n\tau^n)_{k,j}/\delta t = -\,(F^q_{k+1,j} - F^q_{k,j} + G^q_{k,j+1} - G^q_{k,j})^{n+1/2} \tag{33}$$

where $\tau_{k,j}$ is the zone volume and F^q and G^q are the time-centered fluxes at the faces of the zone at k,j in the axial and radial directions, respectively. Note that since q is assumed to be located at zone centers and at time-level n, interpolation and extrapolation procedures are in general required to compute the value of q at zone faces and at time-level n+1/2. A variety of such procedures have been developed over the years; indeed, the history of numerical Eulerian hydrodynamics is largely concerned with devising accurate estimates for the fluxes while insuring numerical stability. We employ Van Leer's (1977) second-order accurate monotonic interpolation scheme for the spatial centering, and extrapolate q along the relative streamline given by $dx/dt = v-v_g$ for the temporal centering. This is illustrated below for a model one-dimensional problem, and then applied to our two-dimensional problem.

4.1 Van Leer monotonic interpolation scheme

Consider a one-dimensional strip of zones with index i, and a set of zone averages $\{q_i\}$ as in Fig. 2. Second-order accurate interpolation functions q(x) result from assuming a piecewise linear distribution of q within zones $q_i(\chi) = q_i + dq_i\chi$, $-1/2\le\chi\le1/2$, where χ is the normalized distance from the zone's center. From this definition, it is clear that q_i is a zone average, since $\int q_i(\chi)d\chi=q_i$. Van Leer's (1977) monotonic interpolation scheme chooses the largest (in absolute magnitude) dq_i such that $q_i(-1/2)$ and $q_i(1/2)$ do not exceed the neighboring zone averages $q_{i\pm1}$. In the event that q_i is a local extremum, $dq_i=0$. Mathematically, letting $\Delta q_i\equiv q_i-q_{i-1}$, then

$$dq_i = \begin{cases} 2\Delta q_i\Delta q_{i+1}/(\Delta q_i+\Delta q_{i+1}), & \Delta q_i\Delta q_{i+1}>0, \\ 0, & \Delta q_i\Delta q_{i+1}\le 0. \end{cases} \tag{34}$$

The flux of q at interface i is then taken to be

$$F^q_i = q^*_i(v-v_g)_i^{n+1/2}\Sigma_i^{n+1/2}, \tag{35}$$

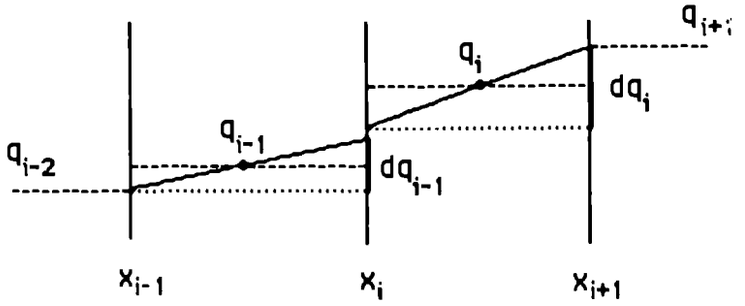

Fig. 2 Van Leer monotonic interpolation scheme. Zone interfaces are at x_i, and zone averages q_i are at zone centers. Piecewise-linear interpolation function (solid lines) is constructed such that the interface values do not exceed the neighboring zone averages (dashed lines). Zone differences dq_i are given by eq. (34).

where $\Sigma_i^{n+1/2}$ is the time-centered area of the zone face, and q^*_i is the upstream interpolated value of q given by (Fig. 2)

$$q^*_i = \begin{cases} q_{i-1} + (\Delta x_{i-1} - \delta_i) dq_{i-1}/(2\Delta x_{i-1}), & \delta_i \geq 0, \\ q_i - (\Delta x_i + \delta_i) dq_i/(2\Delta x_i), & \delta_i < 0, \end{cases} \qquad (36)$$

where $\delta_i = (v - v_g)_i^{n+1/2} (\delta t/2)$, and $\Delta x_i \equiv x_{i+1} - x_i$.

The physical picture behind this prescription is illustrated in Fig. 3. To first order, the value of q on the interface at the half time-level is that obtained by passive advection of q^n for half a timestep. The relative streamline has slope $Dx/Dt - dx/dt \equiv v - v_g$, hence eq. (36). Since q^*_i appears in eq. (33) through a centered difference, the method is formally second-order accurate.

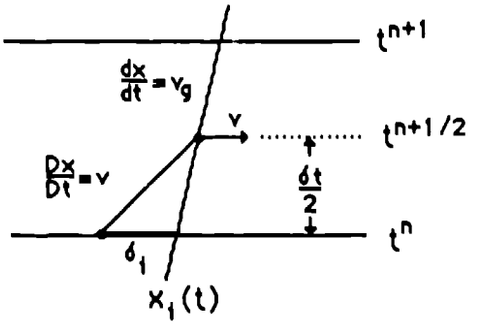

Fig. 3 Upwind procedure for computing time-centered value q^*_i in the flux F^q_i. The relative streamline is tracked upstream from the half time-level a distance $\delta_i = (v - v_g)\delta t/2$. q^*_i is then computed using the interpolation function of Fig. 2 via eq. (34).

4.2 Continuity equation

Letting q=ρ in eq. (33), we have the finite difference form to eq. (7), where the fluxes are given by

$$F^{\rho}_{k,j} = \rho^{*}_{k}(U^{q}_{k,j}-U_{g,k})(R_{j+1/2}\Delta R_{j+1/2})^{n+1/2}, \tag{37}$$

$$G^{\rho}_{k,j}= \rho^{*}_{j}(V^{q}_{k,j}-V_{g,k})\, R^{*}_{k,j}\Delta Z^{\,n+1/2}_{k+1/2}. \tag{38}$$

Here, ρ^{*}_{k} and ρ^{*}_{j} are the interpolated values of density, with the index denoting the direction (i.e., Z or R) of interpolation.The time-centered coordinates are given by

$$R^{n+1/2}_{j+1/2} = R^{n}_{j+1/2} + (\delta t/4)(V_{g,j+1}+V_{g,j}), \tag{39}$$

$$\Delta R^{n+1/2}_{j+1/2} = \Delta R^{n}_{j+1/2} + (\delta t/2)(V_{g,j+1}-V_{g,j}), \tag{40}$$

$$\Delta Z^{n+1/2}_{k+1/2} = \Delta Z^{n}_{k+1/2} + (\delta t/2)(U_{g,k+1}-U_{g,k}), \tag{41}$$

and

$$R^{*}_{k,j}= R^{n}_{j} - (\delta t/2)(V^{q}_{k,j}-V_{g,j}), \tag{42}$$

the mean radius of the advected fluid element.

The new density is then simply

$$\rho^{n+1}_{k,j} = \rho^{n}_{k,j}\tau^{n}_{k,j}/\tau^{n+1}_{k,j}, \tag{43}$$

where

$$\tau^{n(+1)}_{k,j} = (R_{j+1/2}\Delta R_{j+1/2}\Delta Z_{k+1/2})^{n(+1)}. \tag{44}$$

4.3 Consistent advection and the local conservation of angular momentum

In principle, the procedure just described for transporting the mass density could be applied to all the other densities in the problem - E, S, T and A - with out any further thought, remembering only that we must define appropriate control volumes for the linear momentum components S and T. In the case of angular momentum transport, however, such an approach is far from optimal, and in some circumstances, has disasterous results on the local conservation of angular momentum (see Fig. 4). The concern about local conservation of angular momentum in rotating protostar collapse calculations led to the notion of *consistent advection* (Norman, Wilson and Barton 1980), in which the angular momentum flux is calculated by multiplying the mass flux with a best guess for the specific angular momentum of the advected fluid element. Thus, angular momentum is transported consistently with the mass. The physical rationale for this is that K≡A/ρ is conserved along a fluid streamline in axial symmetry in the absence of viscous torques, and therefore the spatial interpolation should be

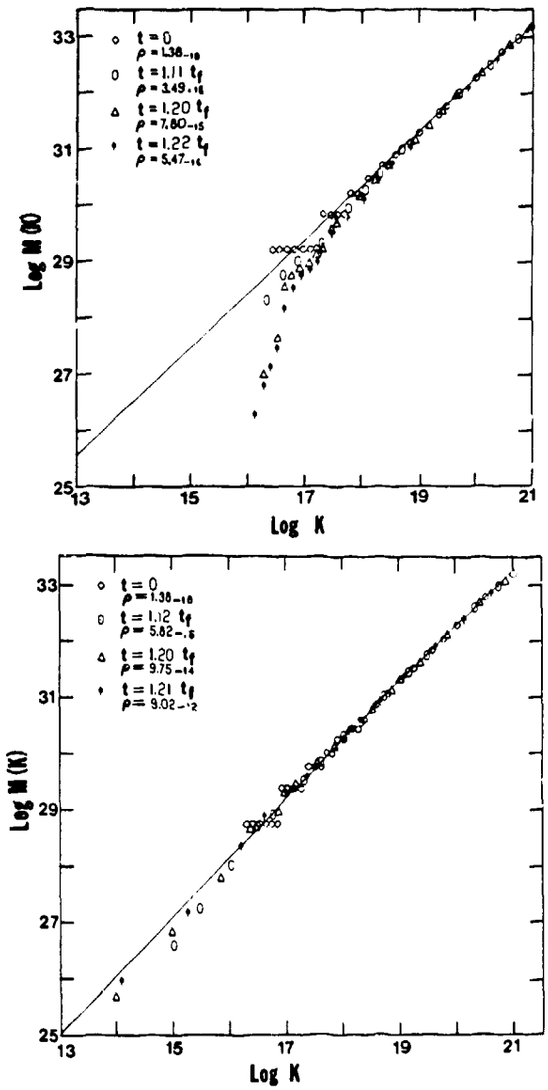

Fig. 4 Numerical diagnostic of the local conservation of angular momentum in a gravitationally collapsing rotating protostellar cloud showing the importance of consistent advection. Local conservation of angular momentum is monitored through changes in the specific angular momentum spectrum, defined as $M(K)=\int^K dM(k)$, where $K=\Omega R^2$ and dM(k) is the mass at specific angular momentum k. M(K) is a constant of the motion for inviscid axisymmetric flow, therefore any changes in the spectrum show numerical redistribution of angular momentum. **a)** Significant evolution of the specific angular momentum spectrum results from using the highly innacurate donor-cell procedure. Various symbols correspond to the indicated times, measured in initial freefall times. **b)** Same collapse problem computed using second-order accurate consistent advection procedure described in Sec. 4.3 showing improved local conservation of angular momentum. From Norman, Wilson and Barton (1980).

performed on K rather than A, since K is the physically more relevant quantity.

Letting q=A in eq. (33), we have the finite-difference form of

$$d/dt \int A \, d\tau = - \int A \, (v - v_g) \cdot d\mathbf{\Sigma}, \tag{45}$$

describing conservation of angular momentum, where the fluxes are given by

$$F^A_{k,j} = K^*_k \, F^\rho_{k,j}, \tag{46}$$

$$G^A_{k,j} = K^{**}_j \, G^\rho_{k,j}, \tag{47}$$

with K^*_k being the interpolated value of specific angular momentum in the axial direction, and K^{**}_j is computed by interpolating on the flattest of three angular quantities. Defining

$$K_{k,j} = A_{k,j} / \rho_{k,j}, \tag{48}$$

$$W_{k,j} = K_{k,j} [3R_{j+1/2} / (R^2_{j+1} + R_{j+1}R_j + R^2_j)], \tag{49}$$

$$\Omega_{k,j} = K_{k,j} [2 / (R^2_{j+1} + R^2_j)], \tag{50}$$

that is, the values of K, W and Ω assuming they are uniform in a zone, then we take

$$K^{**}_j = \begin{cases} \Omega^*_j (R^*_{k,j})^2 & \text{if } |d\Omega_j / \Omega_{k,j}| \text{ smallest,} \\ W^*_j (R^*_{k,j}) & \text{if } |dW_j / W_{k,j}| \text{ smallest,} \\ K^*_j & \text{if } |dK_j / K_{k,j}| \text{ smallest.} \end{cases} \tag{51}$$

Here, the single asterisk means values determined by monotonic interpolation as described in Sec. 4.1.

An equation analogous to eq. (43) is then solved to find A^{n+1}.

Likewise are temperature and velocity intrinsic properties of fluid elements, and therefore it makes physical sense to construct fluxes of energy and momentum density by multiplying the mass flux by the appropriate interpolated values of ε, U and V, even though these quantities are not conserved. We follow this procedure here. A numerical justification is that a product of monotonic functions is monotonic; e.g., $E^*=\rho^*\varepsilon^*$, while the same is not true of the quotient of monotonic functions; e.g., $\varepsilon^*=E^*/\rho^*$, which could lead to difficulties if, for example, the physical model contained a source term with a strong nonlinear dependence on ε. As we shall see in the next section, consistent advection of momentum is manditory in the vicinity of fluid interfaces, where the momentum density may jump by orders of magnitude but the normal velocity component is continuous.

Letting q=E in eq. (33), we have the finite-difference form of eq. (9), where

the fluxes are given by

$$F^{E}_{k,j} = \varepsilon^{*}_{k} F^{\rho}_{k,j}, \tag{52}$$

$$G^{E}_{k,j} = \varepsilon^{*}_{j} G^{\rho}_{k,j}, \tag{53}$$

where ε^{*}_{k} and ε^{*}_{j} are computed in the same fashion as the interpolated densities. An equation analogous to eq. (43) is then solved to find E^{n+1}.

4.4 Momentum transport

Letting q=S and T in eq. (33), we have the finite-difference approximation to eq. (8), where now S and T are interpreted as zone averages over their respective control volumes. Since S and T are face-centered quantities, their control volumes are offset by a half zone-width in the Z and R directions, respectively, from the control volume centered on ρ. The situation is illustrated in Fig. 5. The momentum fluxes are computed by multiplying an appropriate average of the mass flux by the appropriate velocity component interpolated to the zone face. Thus, to transport S, we have (cf. Fig. 5a)

$$F^{S}_{k+1,j} = (F^{\rho}_{k,j} + F^{\rho}_{k+1,j})\, U^{*}_{k+1} / 2, \tag{54}$$

$$G^{S}_{k,j+1} = (G^{\rho}_{k-1,j+1} + G^{\rho}_{k,j+1})\, U^{*}_{j+1} / 2. \tag{55}$$

An additional step is involved in the radial momentum transport calculation. Specifically, because the control volume for T is offset in the radial direction from the mass control volume (cf. Fig 5b), the radial area factors are removed from the mass fluxes prior to averaging, and then the offset radial area factors are multiplied back in. Thus, we have

$$F^{T}_{k+1,j} = [(F^{\rho}/\Sigma)_{k+1,j} + (F^{\rho}/\Sigma)_{k+1,j-1}]\, \Sigma^{T}_{j} V^{*}_{k+1} / 2, \tag{56}$$

$$G^{T}_{k,j+1} = [(G^{\rho}/R^{*})_{k,j+1} + (G^{\rho}/R^{*})_{k,j}]\, R^{*}_{k,j+1/2} V^{*}_{j+1} / 2, \tag{57}$$

where

$$\Sigma^{T}_{j} = (R_{j}\, \Delta R_{j})^{n+1/2}, \tag{58}$$

$$R^{*}_{k,j+1/2} = R^{n}_{j+1/2} - (\delta t/4)(V^{q}_{k,j} + V^{q}_{k,j+1} - V_{g,j} - V_{g,j+1}), \tag{59}$$

with analogous expressions to eqs. (39,40) for the time-centered quantities appearing in eq (58).

The new momentum densities S^{n+1} and T^{n+1} are computed in analogy to eq (43) using the appropriate momentum control volumes.

5. FLUID INTERFACES

A fluid interface is a numerical representation of a boundary between fluids

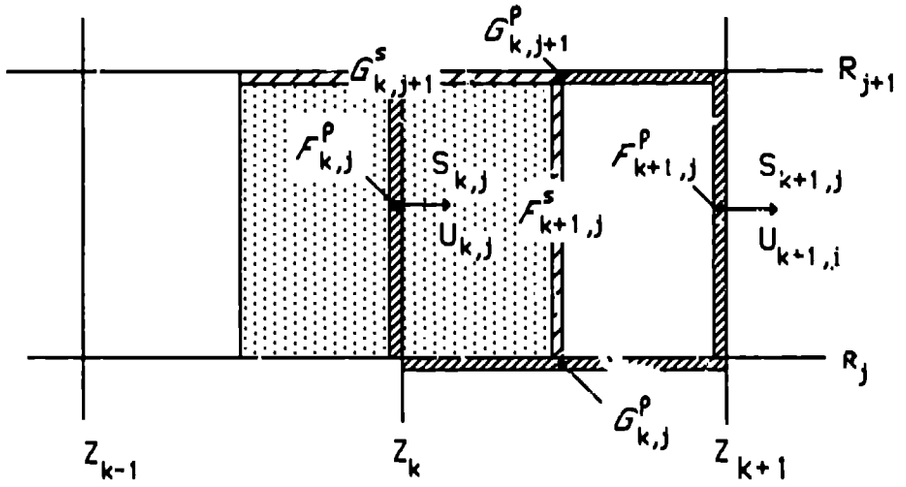

Key: ☐ mass control volume ⬚ Z-momentum control volume
▨ advected mass ▨ advected Z-momentum

Fig. 5a Mass and momentum control volumes and fluxes for the transport of S, the Z-momentum density.

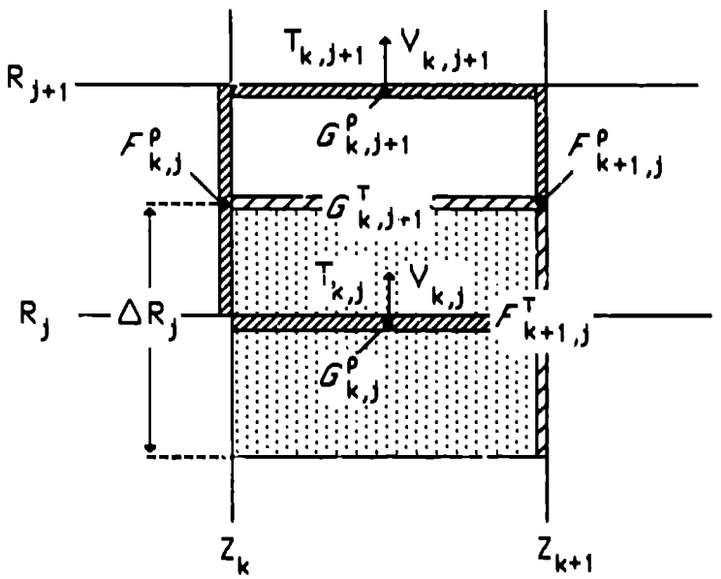

Fig. 5b Mass and momentum control volumes and fluxes for the transport of T, the R-momentum density. Otherwise, key as above.

of different material properties in Eulerian hydrodynamics computations. Some examples of material properties that one might like to distinquish using interfaces are the constitutive properties of the fluid (e.g., equation of state and opacity), the underlying physical model, or simply density or temperature. Since we are modeling ideal (i.e., inviscid) gas flow, such boundaries are idealized as contact discontinuites, and the function of the interface is to prevent the numerical diffusion of the adjacent gas elements into one another. Examples of this technique's use are given in Sec. 8 on several problems in astrophysics where we would like to preserve and track the interface between a hot diffuse medium and a cold dense medium.

Operationally, each material in the calculation is labeled. The label is used as an indicator of material properties. A *mixed* zone is a zone containing more than one material. Zones containing a single material are called *clean* zones, which are advanced in time as described in Secs. 3 and 4. In this section we describe the algorithms we use to advance mixed zones, which were developed by J.M. LeBlanc of the Lawrence Livermore National Laboratory. But first, we give some background on interface methods in general.

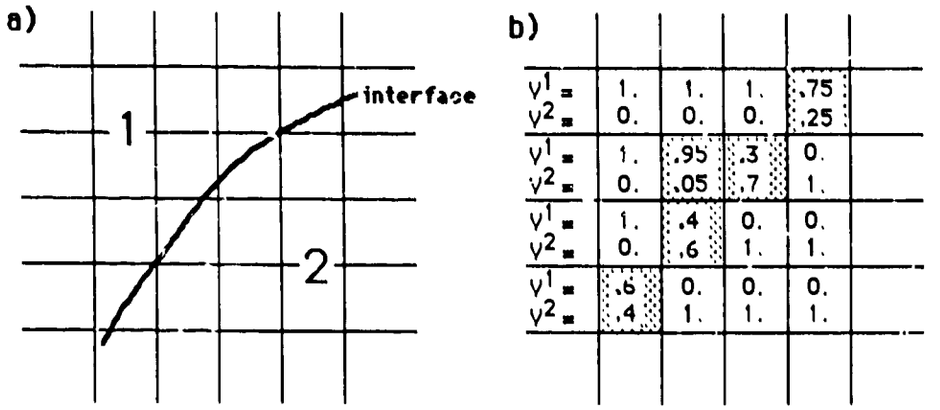

Fig. 6 Numerical representation of a fluid interface on the mesh **a)** by an array of fractional volumes **b)**. Mixed zones are shaded, clean zones are not.

5.1 Method of fractional volumes

The most obvious approach to modeling fluid discontinuites in multidimensional Eulerian calculations is to discretize the surface of reduced dimensionality, such as a set of points approximating a line in a 2-D computation, and then to evolve this surface by solving additional numerical equations approximating the Rankine-Hugoniot jump conditions in its immediate vicinity (see, for example, Richtmyer and Morton 1967, p378). While potentially powerful, this approach has been difficult to implement in an efficient and robust fashion in general-purpose hydro codes, and thus is not commonly used. Recent

progress using advanced programming languages (Glimm 1985) may change this state of affairs, however.

A second and more approximate approach, first developed by deBar (1974) and in extensive use today for handling contact discontinuities, is to represent the global structure of the interface by a function that is defined locally. This function is the fractional volume occupied by each material in a zone, and is denoted V^i, where i is the material index. V^i is a vector of unknowns defined at every zone k,j satisfying the constraint $\Sigma V^i = 1$. In a clean zone containing material with index j, $V^i = \delta^{ij}$, where δ^{ij} is the Kronecker delta. In a mixed zone, more than one fractional volume is nonzero. Fig. 6 illustrates how an interface between two different fluids would be represented on the computional mesh using fractional volumes.

In addition to specifying the fractional volumes of a mixed zone, one also specifies the composition of the mixed zone through its fractional densities of mass, energy and any other fluid property (e.g. specific angular momentum) that may be discontinuous at the interface. The basic tasks of this approach are 1) to reconstruct the global structure of the interface given $V^i_{k,j}$, and 2) to find equations of motion for the fractional volumes and densities that are simple and easy to program, and which give a reasonably accurate discription of the evolution of the interface in a variety of circumstances.

Two basic paths have been followed over the past decade addressing task 1. The first follows the work of deBar (1974) as implemented in the KRAKEN code, in which the position and orientation of the interface within a mixed zone is reconstructed using the distribution of fractional volumes in *all* the adjacent zones (e.g., in a 3 x 3 block of zones in 2-D). The method of LeBlanc is an example of the second approach, whereby the multidimensional problem is reduced to a series of 1-dimensional problems, and only the adjacent zones in 1-D are used to determine the interface position and orientation. A consequence of this reduction is that the interface geometry is no longer unique; that is, its representation within a zone is different in the X and Y passes. The disadvantage of the directional-splitting approach, of which the SLIC method of Noh and Woodward is another example (see Woodward, these proceedings), is a potential loss of accuracy. The advantage is one of considerably simplifying the algorithm and hence the programming task. Surprisingly, the results obtained with splitting compare quite favorably to the KRAKEN approach (Noh and Woodward 1976).

5.2 Method of LeBlanc

We now describe the interface method of LeBlanc as it is implemented in our code. The following quantities are stored for each material i present in a mixed zone:

$$V^i = \tau^i / \tau, \qquad \text{fractional volume,} \tag{60}$$

$$D^i = \rho^i V^i, \qquad \text{fractional mass density,}$$

$$E^i = D^i \varepsilon^i, \qquad \text{fractional internal energy density,}$$

$A^i = D^i K^i$, fractional angular momentum density,

where τ is the volume of the zone, and τ^i, ρ^i, ε^i and K^i are the volume, density, specific internal energy, and specific angular momentum of material i(in this and in subsequent equations, we will suppress the dependence on zone indices k and j).The quantities D^i, E^i and A^i are therefore the densities material i would have if it occupied the entire volume of the zone. It follows from these definitions that

$$1 = \sum_i V^i, \tag{61}$$

$$\rho = \sum_i D^i,$$

$$E = \sum_i E^i,$$

$$A = \sum_i A^i,$$

where the summation is over the material index i. Only a single set of velocity and momentum density components are carried for a mixed zone, as they are vector quantities.

5.2.1 source step

The pressure in a mixed zone is found by adding the partial pressures:

$$P = \sum_i (\gamma^i - 1) E^i. \tag{62}$$

The angular velocity of a mixed zone is computed as a mass-weighted average of the fractional angular velocities. Thereafter, mixed zones are accelerated like clean zones [cf. eqs. (19,20).]

Heating from artificial viscosity and compressional work is equally partitioned to each material i in a mixed zone:

$$E^{i,q} = (E^q/E)\, E^i,$$

$$E^{i,p} = (E^p/E^q)\, E^{i,q}, \tag{63}$$

where the superscripts refer to steps 2 and 3 of Sec. 3.

5.2.2 transport step

The motion of the interface comes about by transporting the fractional volumes along with the other fractional densities. As in the clean calculation (Sec. 4), transport is done in 1-D sweeps, however a first-order method (donor cell) is used in the vicinity of the interface as an aid to numerical stability.

Consider the triad of zones containing at least one mixed zone as shown in Fig. 7a, and suppose we wish to update the middle zone. Define $\mathfrak{I}^i_{L,R}$ as the fractional fluxes of material i on the left and right, respectively, of this zone, and

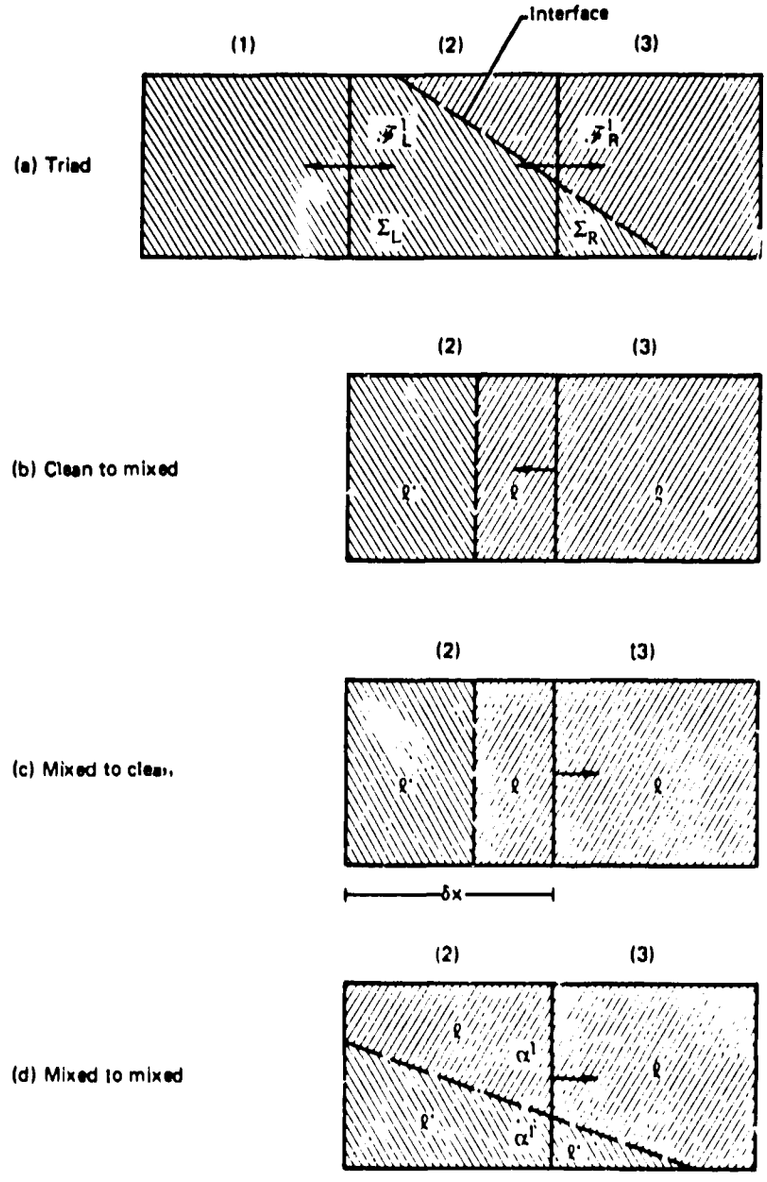

Fig. 7 Advection procedure in a triad of zones containing at least one mixed zone. a) Interface geometry is inferred from the distribution of fractional volumes (cf. Fig. 6). The fractional fluxes $\mathfrak{F}^l$ are derived according to the following three situations. b) Advection from a clean zone to a mixed zone. c) Advection from a mixed zone to a clean zone. d) Advection from a mixed zone to a mixed zone. α^l and $\alpha^{l'}$ are the aperture as defined in eq. (70).

$\Sigma_{L,R}$ as the areas of the left and right zone faces, respectively.The difference equations for the transport of the fractional densities and fractional volumes are then

$$V^{i,n+1} - V^{i,n} = (\Delta^i_R \Sigma_R - \Delta^i_L \Sigma_L) / \tau , \tag{64}$$

$$D^{i,n+1} - D^{i,n} = (\mathfrak{I}^i_R \Sigma_R - \mathfrak{I}^i_L \Sigma_L) / \tau , \tag{65}$$

and similarly for E^i and A^i. Here, the mass flux is defined

$$\mathfrak{I}^i_{L,R} = \Delta^i_{L,R} (D^i/V^i)_d, \tag{66}$$

where the subscript d stands for the donor cell values and the $\Delta^i_{L,R}$ are computed according to the following three cases.

<u>case 1: clean to mixed</u>

Referring to Fig. 7b, in the case of flow from a clean zone containing material l to a mixed zone, we have simply

$$\Delta^i = (U-U_g)\delta t \, \delta^{il} . \tag{67}$$

The donor cell remains clean and the acceptor cell remains mixed.

<u>case 2: mixed to clean</u>

Referring to Fig. 7c, we see that material l may become negative in the donor cell if $|U-U_g|\delta t > (V^l \Delta x)_d$. Therefore

$$\Delta^i = \text{sign } (U-U_g) \min| \, |U-U_g|\delta t , (V^l \Delta x)_d \, |\delta^{il} . \tag{68}$$

If $|U-U_g|\delta t > (V^l \Delta x)_d$, then we take the next material in line according to

$$\Delta^{l'} = \text{sign } (U-U_g) \min| \, |U-U_g|\delta t - \Delta^l , (V^{l'} \Delta x)_d \, |\delta^{il'} , \tag{69}$$

and so on until everything $|U-U_g|\delta t$ behind the flow has been taken. In this case, the donor cell may become clean and the acceptor cell may become mixed.

<u>case 3: mixed to mixed</u>

Referring to Fig. 7d, we define aperatures α^i through which material i may pass as follows:

$$\alpha^i = (V^i_L + V^i_R)/2, \tag{70}$$

Then we have simply

$$\Delta^i = \alpha^i (U-U_g)\delta t . \tag{71}$$

Notice that $\Sigma \alpha^i = 1$, so that the scheme is conservative.

Total densities for the zone are found by summing the fractional densities. If the interface is in a region of the flow with a velocity gradient normal to its surface, then in general $\Sigma V^{i,n+1} \neq 1$, in which case the fractional volumes are renormalized so that they sum to unity. Finally, integrated mass fluxes are computed for use in the linear momentum transport calculation (cf. Sec. 4.4):

$$F^{\rho} = (\sum_{i} \Im^{i})\Sigma/\delta t. \tag{72}$$

5.3 Properties of the interface method

The interface method just described works best on, and in fact was developed for, isolated contact discontinuities in flows with little velocity shear both normal and tangential to the discontinuity's surface. This will not be the case if the discontinuity is interacting with a strong shock or rarefaction wave, nor if it is a *slip* discontinuity.This can be seen by noticing that only one set of velocity components are used to describe both mixed zones and clean zones alike. Indeed, incorporating "fractional velocities" into a such a technique would be difficult because the orientation of the interface is only loosely defined, and one would naturally want to work in terms of discontinuities in the normal and tangential velocity components. By definition, the normal component of velocity is continuous at a contact discontinuity, and therefore in such problems as material boundaries moving normal to their surface, as arise in Rayleigh-Taylor instabilities, one velocity per zone is adequate to give an accurate representation of the interface's motion. In problems with a large amount of slip across the discontinuity, as arise in Kelvin-Helmholtz instabilities, the interface dynamics is driven by the mean flow in which it is embedded. In both cases, the primary function of the fluid interface is to act as a *material separator* , as they were termed originally, preventing numerical diffusion from artificially broadening the discontinuity into several zone-widths.

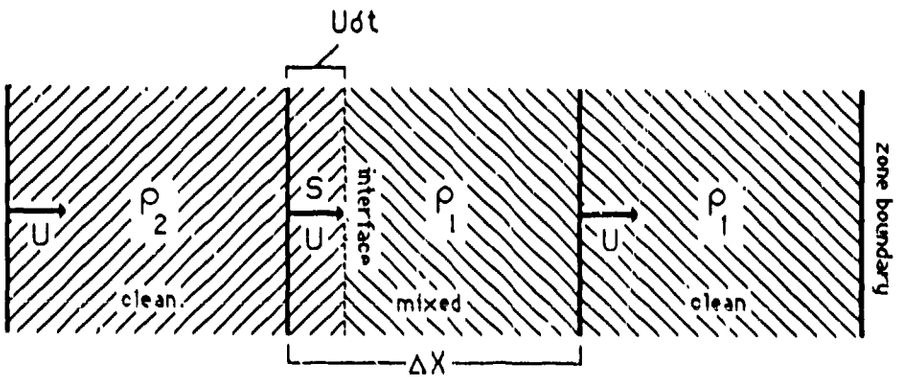

Fig. 8 One-dimensional interface advection in a uniform velocity field U. Discontinuity between $\rho=\rho_1$ and $\rho=\rho_2$ initially coincides with the second-from-the-left zone boundary. Consistent momentum advection (cf. Sec. 4.4) insures that U remains constant despite a large jump in mass and momentum densities.

We shall now demonstrate that the LeBlanc interface method is exact when applied to the uniform advection in 1-D of a discontinuity normal to its surface. Consider three zones as shown in Fig. 8 with a density discontinuity initially coinciding with the zone boundary second from the left. Let the density to the left and right of the discontinuity be ρ_1 and ρ_2, respectively, and let there be a uniform velocity field U pointing to the right. In time δt, the interface will move to the right a distance $U\delta t$, and the new fractional volumes in the middle zone will be $V^1=1- U\delta t/\Delta x$ and $V^2= U\delta t/\Delta x$. This is precisely what eqs. (64) and (67) yield if we set $U_g=0$, $\Sigma=1$ and $\tau=\Delta x$.

In addition, we can show that consistent advection of momentum [cf. Sec. 4.4 and eq. (72)] insures that the uniform velocity field willl be unaltered by the interface treatment. Summing eq. (65) over material index, we find

$$\rho^{n+1} = (1-\sigma)\rho_1 + \sigma\rho_2 , \tag{73}$$

where $\sigma\equiv U\delta t/\Delta x$. Updating the average momentum in the zone centererd about S in Fig. 8, we have from eq. (54)

$$(S^{n+1}-\langle\rho\rangle U)/\delta t = -(\langle\rho\rangle-\rho_2)U^2/\Delta x, \tag{74}$$

or

$$S^{n+1} = [(1-\sigma)\langle\rho\rangle + \sigma\rho_2]U , \tag{75}$$

where $\langle\rho\rangle \equiv (\rho_1+ \rho_2)/2$. It is then easy to show from eqs. (73,74) that

$$U^{n+1} \equiv 2S^{n+1}/ (\rho^{n+1}+ \rho_2) = U. \tag{76}$$

Thus, we have passive advection of the interface with no modification of the background velocity field.

6. SELF-GRAVITY

Sections 3-5 describe the hydrodynamic part of the calculation whereby the fluid variables are advanced from timelevel n to n+1. In problems where the self-gravitational forces of the fluid are important, we must also solve the Poisson equation (4) subject to appropriate boundary conditions in order to determine the gravitational potential at the new timelevel Φ^{n+1}_{kj} which enters in eqs. (19,20).

The boundary values of gravitational potential are computed from a multipole expansion,

$$\Phi_B = -G\sum_l P_l(\mu_B)\, r_B^{-(l+1)} M_l , \tag{77}$$

where the multipole moments are given by

$$M_l = \int d\tau\, \rho(\mathbf{r})\, r^l\, P_l(\mu) . \tag{78}$$

Here **r** is the position vector from the center of the self-gravitating structure, usually at Z=0, R=0; r=|**r**|; μ is the cosine of the angle between the rotation axis and **r**; and P_l are the Legendre polynomials. The subscript B means that these quantities are to be evaluated on the boundary of the computational domain. With assumed equatorial symmetry, the odd moments vanish, and the boundary value at Z=0 becomes $\partial\Phi/\partial Z=0$. In practice only the l=0, 2 and 4 terms are used, which has proven to be adequate if the outer boundary is sufficiently removed from the structure. The boundary value at the axis is, of course, $\partial\Phi/\partial R=0$.

As we generally deal with nonuniform meshes in both coordinate directions which are not spatially periodic, Fourier transform methods to solve eq. (4) are ruled out. Also, direct methods such as Gaussian elimination would be too time-consuming, and hence we must consider iterative techniques. The solution technique for the Poisson equation we use has been described by Black and Bodenheimer (1975), but will be repeated here. The plan is to find the steady-state solution to the diffusion equation

$$\partial\Phi/\partial t = \nabla^2\Phi - 4\pi G\rho^{n+1} , \tag{79}$$

using the ADI method (Peaceman and Rachford 1955) for a series of iterative "timesteps". The time appearing in eq. (79) bears no relation to the physical time of the evolution; the timesteps are chosen to speed convergence.

Let Φ^p be the p^{th} estimate for the gravitational potential, and δt^p be the timestep for the p^{th} iteration. Defining

$$\Delta_Z\Phi_{k,j} \equiv \Phi_{k,j} - \Phi_{k-1,j} , \tag{80}$$

$$\Delta_R\Phi_{k,j} \equiv \Phi_{k,j} - \Phi_{k,j-1} , \tag{81}$$

then Φ^p is advanced to Φ^{p+1} by the following two-step ADI procedure:

$$(\Phi^{p+1/2}-\Phi^p)_{k,j}/\delta t^p = (\Delta_Z\Phi^p{}_{k+1,j}/\Delta Z_{k+1} - \Delta_Z\Phi^p{}_{k,j}/\Delta Z_k)/\Delta Z_{k+1/2}$$
$$+ (R_{j+1}\Delta_R\Phi^{p+1/2}{}_{k,j+1}/\Delta R_{j+1} - R_j\Delta_R\Phi^{p+1/2}{}_{k,j}/\Delta R_j)/(R\Delta R)_{j+1/2} - 4\pi G\rho^{n+1}{}_{k,j} , \tag{82}$$

followed by

$$(\Phi^{p+1}-\Phi^{p+1/2})_{k,j}/\delta t^p = (\Delta_Z\Phi^{p+1}{}_{k+1,j}/\Delta Z_{k+1} - \Delta_Z\Phi^{p+1}{}_{k,j}/\Delta Z_k)/\Delta Z_{k+1/2}$$
$$+ (R_{j+1}\Delta_R\Phi^{p+1/2}{}_{k,j+1}/\Delta R_{j+1} - R_j\Delta_R\Phi^{p+1/2}{}_{k,j}/\Delta R_j)/(R\Delta R)_{j+1/2} - 4\pi G\rho^{n+1}{}_{k,j} . \tag{83}$$

The implicit sweeps generate a set of tridiagonal matrix equation which are solved directly using the well-known technique of "forward sweep, backward

substitution" described by Richtmyer and Morton (1967).

Eqs. (82,83) are solved for $0 \le p \le P-1$, where the iterative timesteps δt^p form a geometric series

$$\delta t^p = \alpha^p \delta t_{max} \; ; \; p=0,1,....,P-1, \tag{84}$$

with

$$\delta t_{max} = \max(Z_{max}^2, R_{max}^2)/4, \tag{85}$$

and

$$\alpha = (\delta t_{min}/\delta t_{max})^{1/(P-1)}, \tag{86}$$

$$\delta t_{min} = \min(\Delta Z_{min}^2, \Delta R_{min}^2)/4 \; . \tag{87}$$

The new potential is given by $\Phi^{n+1}=\Phi^P$. This timestep prescription is constructed in analog to a treatment by Peaceman and Rachford (1955), who solved diffusion in a square, rectangular mesh. The timesteps are chosen to reduce the amplification factors of eqs. (82,83) for modes of wavelength comparable to $(\delta t^p)^{1/2}$.

Convergence is checked by monitoring

$$\chi = \max_{k,j} |\nabla^2\Phi - 4\pi G\rho| \; / \; 4\pi G\rho, \tag{88}$$

which should be $\le 10^{-5}$ to achieve a potential gradient accuracy of about a percent. We find typically that $10^{-6}<\chi<10^{-10}$ if P is approximately half the number of zones in one dimension.

7. TIMESTEP CONTROL

The final operation in the problem cycle is the calculation of a new timestep to be used in the next cycle. Explicit hydrodynamics requires the timestep to satisfy the Courant condition for stability, which for a one-dimensional problem is

$$\delta t \le \min \Delta x/(C+|U|), \tag{89}$$

Where C and U are the local sound speed and flow speed, and the minimum is taken over the entire domain. A simple and effective prescription for multidimensional calculations which we use is

$$\delta t^{n+1} = b \; [\max_{k,j}(\sum_{i=1}^{3} \delta t_i^{-2}) + \delta t_4^{-2}]^{-1/2} \; , \tag{90}$$

where b is the safety factor, usually ≈ 0.5, and the δt_i are defined for each zone k,j as follows:

$$\delta t_1 = \min (\Delta Z, \Delta R)/C, \tag{91}$$

$$\delta t_2 = \Delta Z/|U-U_g| \; , \tag{92}$$

$$\delta t_3 = \Delta R/|V-V_g| \,. \tag{93}$$

The artificial viscosity also limits the timestep, since Q^{ZZ} and Q^{RR} are used to form a momentum diffusion problem. For an explicit diffusion scheme the timestep is limited by

$$\delta t \le \Delta x^2 / 4\nu \tag{94}$$

where ν is the kinematic viscosity. A comparison of eqs. (21,22,24 & 25) with $C_1=0$ to the Navier-Stokes equation shows the numerical kinematic viscosity to be

$$\nu^{ZZ} = \Delta Z(C_2 Q^{ZZ}/\rho)^{1/2} = C_2|\Delta U|\Delta Z \,, \tag{95}$$

$$\nu^{RR} = \Delta R(C_2 Q^{RR}/\rho)^{1/2} = C_2|\Delta V|\Delta R \,, \tag{96}$$

thus we define a fourth timestep for zones with nonzero Q,

$$\delta t_4 = \min\,(\Delta Z/4C_2|\Delta U|,\ \Delta R/4C_2|\Delta V|) \,. \tag{97}$$

Finally, the timestep is limited to a 30 percent increase per cycle to maintain accuracy when the system makes abrupt dynamical changes, yet may decrease by an arbitrary amount in order to maintain numerical stability.

8. NUMERICAL EXAMPLES

In this section we illustrate the use of our numerical techniques on a number of problems of astrophysical interest involving static and dynamic fluid interfaces.

8.1 Self-gravitating isothermal clouds

The picture of a cold, dense isothermal cloud in pressure equilibrium with a hot intercloud medium is a paradigm for the interstellar medium that is often used as initial conditions for calculations of gravitational collapse and star formation. Unlike self-gravitating equilibria with polytropic equations of state, isothermal equilibria are infinite in spatial extent unless truncated at some finite radius with a finite boundary pressure, such as would be provided by a hot intercloud medium. Such truncated self-gravitating isothermal equilibria possessing zero angular momentum are called Bonner-Ebert spheres, named after the men who first determined their structure (Bonner 1956; Ebert 1955). The rotating analogs to the Bonner-Ebert spheres were first investigated by Norman (1980) using the hydrodynamic techniques described above, and subsequently by Stahler (1983) and Hachisu and Eriguchi (1984) using hydrostatic codes.

In the hydrodynamic approach, a fluid interface was used to delineate the cloud-intercloud boundary, which is a free boundary. As initial conditions for the calculation, Norman assumed a constant density and temperature sphere with a specified rotation law embedded in a constant pressure background. The initial

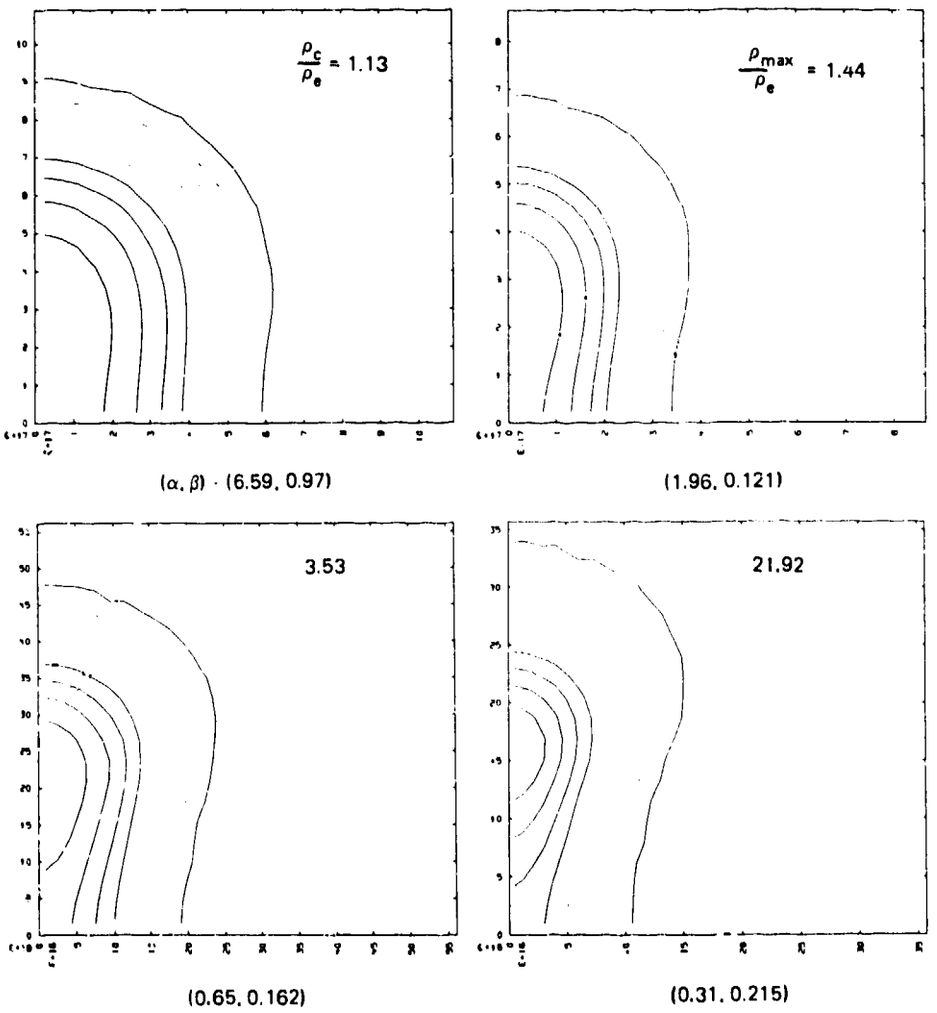

Fig. 9 Equidensity contours of rotating, isothermai equilibria of constant mass, angular momentum and distribution of angular momentum for several values of α=|internal energy / gravitational energy| and β=|rotational energy / gravitational energy| (in parenthesis). One quadrant is displayed and the rotation axis is horizontal. The lower, right-hand model is near criticality to gravitational collapse. The cloud boundary (outermost solid line) is described by a fluid interface. From Norman (1980).

conditions were then evolved to equilibrium hydrodynamically with a velocity-dependent damping term added to the momentum equation in order to hasten the approach to equilibrium. Once equilibrium was reached, the cloud temperature was slowly decreased, generating a "cooling sequence" of quasi-static isothermal spheroids of constant mass, angular momentum and its distribution. During the initial relaxation phase and cooling phases, the intercloud medium was not evolved hydrodynamically, but rather was kept at constant density and pressure.

Fig. 9 shows four equilibria from a cooling sequence initiated with a sphere whose angular velocity was ten times higher at its center than at its edge. The fluid interface is indicated by the outermost solid line. A consequence of this angular momentum distribution is toroidal equilibria for $\alpha<1$, where α is the ratio of the cloud's internal energy to its gravitational self-energy. As the temperature is further decreased, the minimum α for stable equilibrium α_c is encountered. Below α_c the cloud is dynamically unstable to gravitational collapse. Collapse is computed numerically at constant cloud temperature without the damping term in the equation of motion. Fig. 10 shows the cloud structure well into the collapse phase when the peak density on the toroidal axis exceeds 10^3 times the edge value. For a complete discussion of the collapse dynamics and its dependence on angular momentum distribution, the reader is referred to Norman (1980).

8.2 Supersonic jets

Calculations of supersonic jets of the sort displayed in Plate 1 have been performed in connection with radio galaxy studies and their associated radio jets (Norman et al. 1982; Norman, Winkler and Smarr 1983,1985; Norman, Smarr and Winkler 1984; Smarr, Norman and Winkler 1984; Smith et al. 1985). The calculations are performed in 2-D axisymmetry neglecting self-gravity and rotation. Initially, the computational domain is filled with a uniform, static background gas which is to represent the intergalactic medium surrounding the radio galaxy. Subsequently, a perfectly collimated supersonic beam of gas is continuously injected through an area on the domain boundary, and its interaction with the ambient gas is computed. The beam's incident pressure is chosen to match the undisturbed ambient pressure, whereas its incident density and velocity are varied from evolution to evolution. A fluid interface (shown in black) is used to track the contact discontinuity seperating the jet gas from the ambient gas.

Plate 1a shows the establishment of a Mach 3 jet with an input density of 10% the background density. A characteristic of low density jets is that as they propagate, they enshroud themselves in a cocoon of gas that has "splashed back" from the leading end of the jet. The cocoon is generally less dense and hotter than the beam gas because of shock-heating at the terminal shock front. This can be seen as a difference in colors between the central beam (green) and cocoon (blue) in Plate 1, where different densities have been assigned different colors according to the scale accompanying Plate 2. As can bee seen in Plates 1b-d, the jet boundary is subject to Kelvin-Helmholtz instabilities which lead to turnover and mixing of the jet and ambient gases. The fluid interface allows one to follow these interfacial instabilities into the nonlinear regime with a minimum of numerical diffusion. A wealth of hydrodynamical detail can be extractred from

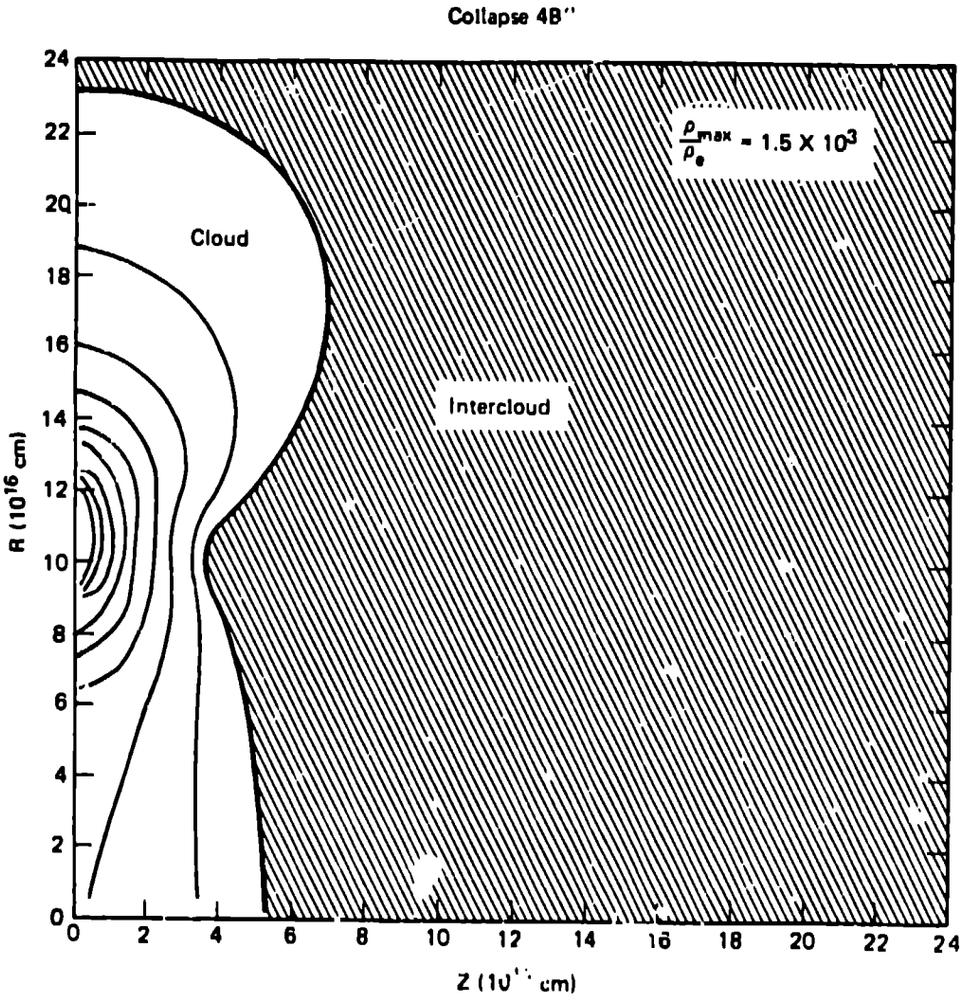

Fig. 10 Gravitational collapse from the equilibrium toroidal cloud shown in Fig. 9d. The calculation was halted at a density contrast of 1.5×10^3, when the zoning resolution became inadequate to follow the subsequent condensation. Isodensity contours are plotted. From Norman (1980).

the calculations using the color imaging techniques described by Winkler and Norman in these proceedings. A comprehensive overview of the key physical results is given in Smarr, Norman and Winkler (1984).

Plate 2 illustrates a second application of our numerical techniques to the propagation of supersonic gas jets. In this calculation, 2-D cartesian geometry is assumed so that nonaxisymmetric "kink" instabilities can be studied. The numerical procedure is idendical to the axisymmetric jet calculations described above, except now the jet is admitted with a transverse velocity component which varies sinusoidally in time according to

$$v_y(t) = 0.05\, v_x \sin\omega_r t,$$

where ω_r satisfies Woodward's resonance condition (Woodward, these proceedings) for the fastest-growing unstable mode

$$\omega_r = \pi v_x (M^2-1)^{-1/2}/W$$

where v_x is the beam velocity, M is its internal Mach number and W is the slab width. Plates 2a-d show the rapid growth of the kink instability and its disruptive effect on the directed bulk flow.

8.3 Blastwaves in exponential atmospheres

A strong point explosion in a plane-stratified exponential atmosphere presents some interesting phenomena not found in the Taylor-Sedov type blastwaves produced in a uniform atmosphere. Plate 3 illustrates these phenomena. At t=0, the background gas is distributed according to

$$\rho(Z) = \rho_0 \exp(-Z/h(Z))$$

$$T(Z) = T_0$$

and in hydrostatic equilibrium with the gravitational potential given by

$$\Phi(Z) = \Phi_0 - RT_0 \ln(\rho/\rho_0).$$

h(Z) is the local scale height given by

$$h(Z) = h(Z_c) + a(Z-Z_c),$$

where Z_c is the height of the explosion above the midplane. Although the problem is scale-free, the following astrophysical numbers were used: $\rho_0 = 1.67\times10^{-24}$ g cm^{-3}, $T_0 = 500$K, $Z_c = 1.4\times10^{20}$ cm, $h(Z_c) = 4.21\times10^{19}$ cm, $a = 0.125$ cm^{-1}. A sphere of high temperature ($T_s = 4\times10^{10}$K) and low density ($\rho_s = 6\times10^{-26}$ g cm^{-3}) is emplaced at $Z = Z_c$ with initial radius $r_s = 10^{19}$ cm. A fluid interface seperates the high pressure "driver gas" from the constant temperature background gas. The computational domain spans 6×10^{19} cm $\le Z \le 3.9\times10^{20}$ cm, $0 \le R \le 1.1\times10^{20}$ cm. The subsequent evolution is computed assuming a $\gamma = 5/3$ adiabatic equation of state in both gases.

Plate 3a shows the color-coded entropy distribution shortly after the explosion begins. The distribution of colors in the atmosphere indicates a stable entropy stratification. The red circular region is the high entropy explosion gas that has been shocked by the expanding blastwave. As the blastwave barely extends over one atmospheric scale-height at this time, it is still circular. Plate 3b shows how the blastwave distorts and becomes egg-shaped as it samples different regions of the stratified pressure distribution. The upper apex of the blastwave propagates the fastest since it is following the steepest pressure gradient. Plate 3c and 3d show blastwave "breakout" as first predicted by Kompaneets (1960), and the subsequent buoyant rise of the hot bubble. Note the growth of Rayleigh-Taylor instabilities on the leading edge of the bubble, indicating the necessity of using a fluid interface in this calculation.

8.4 Twin-exhaust jets

As a final example, we consider the production of jets via the Blandford-Rees (1974) Twin-Exhaust mechanism. This mechanism was first proposed to account for the production of twin jets in the nuclei of radio galaxies, and is currently being applied to jet production by protostars embedded in molecular clouds in our own galaxy (Königl 1982). The model holds that if a continuous source of hot, buoyant gas is established in a relatively colder, denser background gas that is gravitationally confined, then the buoyant gas will preferentially escape along the path or paths of least resistance; i.e., parallel to the steepest pressure gradient, which in a radio galaxy nucleus could be taken to be along the minor axis of a rotationally-flattened central gas cloud. According to this model, the boundary between the cold confining gas and the buoyant outflowing gas would naturally assume the shape of a deLaval nozzle, which would accelerate the outflow to supersonic speeds and collimate it into jets. This is manifestly a two-fluid problem requiring a dynamic fluid interface to study the formation and stability of the flow channel boundary.

Plate 4 illustrates the nozzle formation process. The confining atmosphere is initially isothermal, plane-stratified and in hydrostatic equilibrium. The density and hence pressure distribution is a power-law with a central plateau given by

$$\rho(Z) = \rho_0 / [1+(Z/h)^2]$$

$$P(Z) = (\gamma-1)\rho(Z)\varepsilon_0,$$

where ρ_0 and ε_0 are the midplane density and specific internal energy, respectively. Hot gas is continuously created in a spherical source region of radius h/10 with zero velocity at a mass rate m with specific internal energy ε_j. Both fluids were assumed to obey $\gamma=5/3$ ideal gas equations of state. The following dimensionless quantities define the evolution:

$$\lambda = m\varepsilon_j / \rho_0\varepsilon_0^{3/2}h^2$$

$$\theta = \varepsilon_j / \varepsilon_0.$$

This example illustrates an energetic (λ=2) source of hot (θ=100) gas, which we had previously determined to be susceptible to Rayleigh-Taylor instabilities (Norman et al. 1981). The computational domain spans $0 \le Z \le 10h$, $0 \le R \le 10h$.

Plate 4a shows the initial bubble of hot gas inflated by the central source. Gas temperature is color-coded such that high temperatures are red and low temperatures are blue. The bubble is elongated in the direction of the pressure gradient as its size exceeds the plateau scale-length h. Since the interface between the bubble gas and the background gas is Rayleigh-Taylor unstable, any kinks or ripples on the bubble surface will be amplified by the instability. The growth of these instabilities in subsequent frames is tracked with our numerical fluid interface, shown in black.

Plates 4b and 4c show the establishment of the cavity-nozzle-jet structure. The throat of the nozzle forms as dense Rayleigh-Taylor "fingers" penetrate the bubble from the side and converge toward the axis. As the throat necks down, tha cavity inflates with subsonic gas (Plate 4d), and now the top of the cavity develops the characteristic Rayleigh-Taylor "spike and bubble" structure. The dense spikes merge on axis in Plate 4e forcing the jet gas to flow out in an annular region. The annular jet breaks through the layer of dense gas seen in blue in Plate 4e to form the continuous diverging jet of Plate 4f. The jet has an embedded spindle of dense gas along its axis of symmetry, which is slowly being blown downstream by the jet ram pressure.

Further numerical evolutions of this sort are described in Norman et al. (1981), and an analytic discussion of the flow stability is given in Smith et al. (1983). The relevance of these calculations to jet formation in active galactic nuclei is discussed in Smith et al. (1981).

REFERENCES

Black, D.C. & Bodenheimer, P. 1975, Ap. J. 199, p619.

Blandford, R.D. & Rees, M.J. 1974, Mon. Not. Roy. Astron. Soc. 169, p395.

Bonner, W.B. 1956, Mon. Not. Roy. Astron. Soc. 116, p351.

deBar, R. 1974, *Fundamentals of the KRAKEN code*, Lawrence Livermore National Laboratory Internal Report UCIR-760.

Ebert, R. 1955, Zs. f. Astrophys. 37, p217.

Glimm, J. 1984, Courant Institute Preprint.

Hachisu, I. & Eriguchi, Y. 1984, Max-Planck-Institut f. Astrophysik preprint No. 149.

Kompaneets, A.S. 1950, Soviet Phys. Doklady 5, p46.

Konigl, A. 1982, Ap. J. 261, p115.

Noh, W.H. & Woodward, P.R. 1976, in *Proceedings of the 5th International Conference on Numerical Methods in Fluid Dynamics*, (Springer Verlag: New York).

Norman, M.L. 1980, Ph.D. dissertation, University of California, Davis; Lawrence Livermore National Laboratory report UCRL-52946.

Norman, M.L., Smarr, L., Wilson, J.R. & Smith, M.D. 1981, Ap. J. 247, p52.

Norman, M.L., Smarr, L., Winkler, K.-H.A. & Smith, M.D. 1982, Astron. Astrophys. 113, p285.
Norman, M.L., Smarr, L. & Winkler, K.-H.A. 1984, in *Numerical Astrophysics*, ed. J. Centrella, J. LeBlanc & R. Bowers, (Jones and Bartlett: Portola Valley, CA.).
Norman, M.L., Wilson, J.R. & Barton, R. 1980, Ap. J. 239, p968.
Norman, M.L., Winkler, K.-H.A. & Smarr, L. 1983, in *Astrophysical Jets*, ed. A. Ferrari & A.G. Pacholczyk, (Reidel:Dordrecht).
Norman, M.L., Winkler, K.-H.A. & Smarr, L. 1985, in *Physics of Energy Transport in Extragalactic Radio Sources*, ed. A. Bridle & J. Eilek, NRAO Conference Proceedings No. 9.
Richtmyer, R.D. & Morton, K.W. 1967, *Difference Methods for Initial-Value Problems*, (Interscience:New York), p198.
Smarr, L., Norman, M.L. & Winkler, K.-H.A. 1984, Physica D 12, p83.
Smith, M.D., Smarr, L., Norman, M.L. & Wilson, J.R. 1981, Nature 293, p277.
Smith, M.D., Smarr, L., Norman, M.L. & Wilson, J.R. 1983, Ap. J. 264, p432.
Stahler, S. (1983), Ap. J. 268, p165.
vanLeer, B. 1977, J. Comp. Phys. 23, p276.

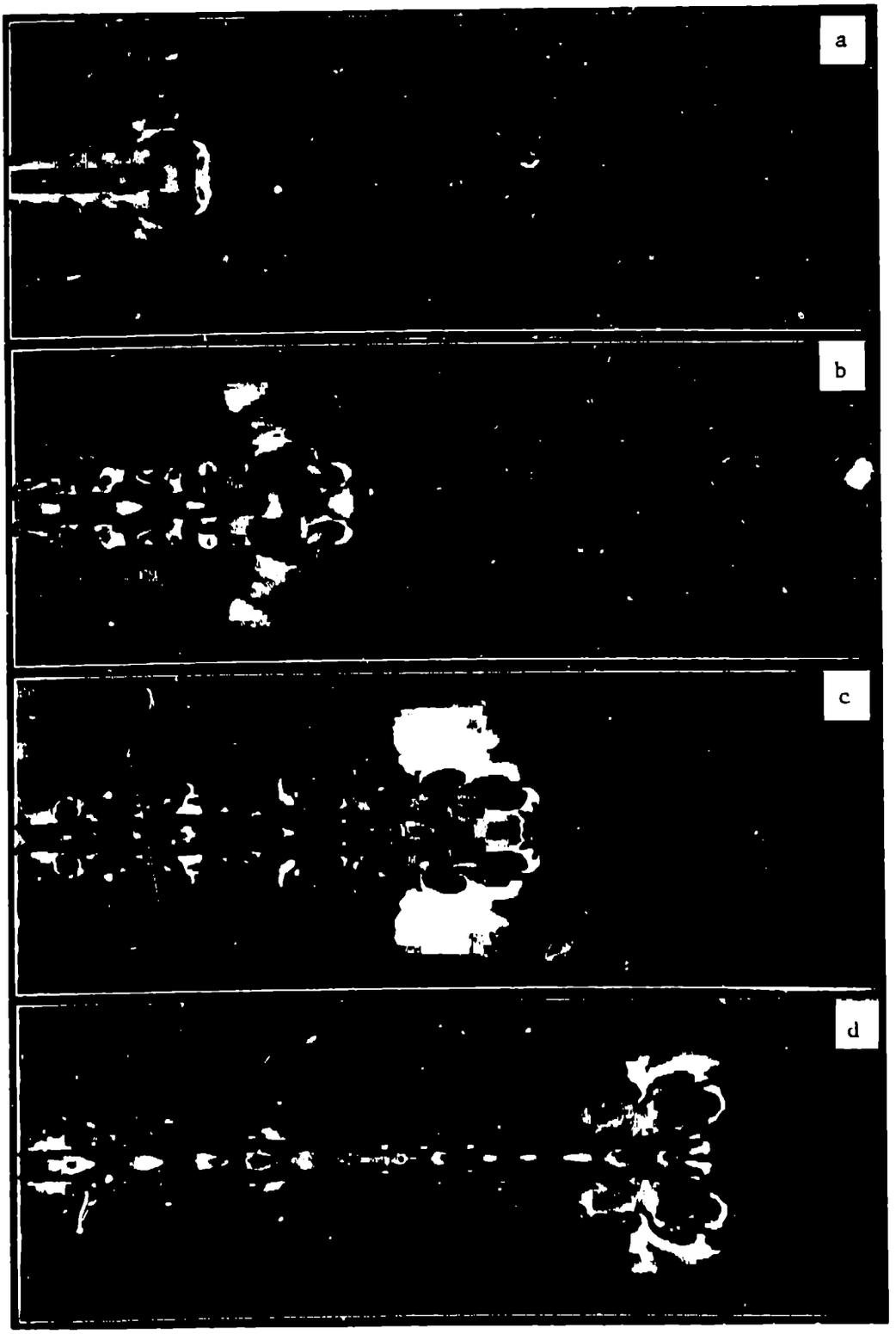

Plate 1

Plate 2

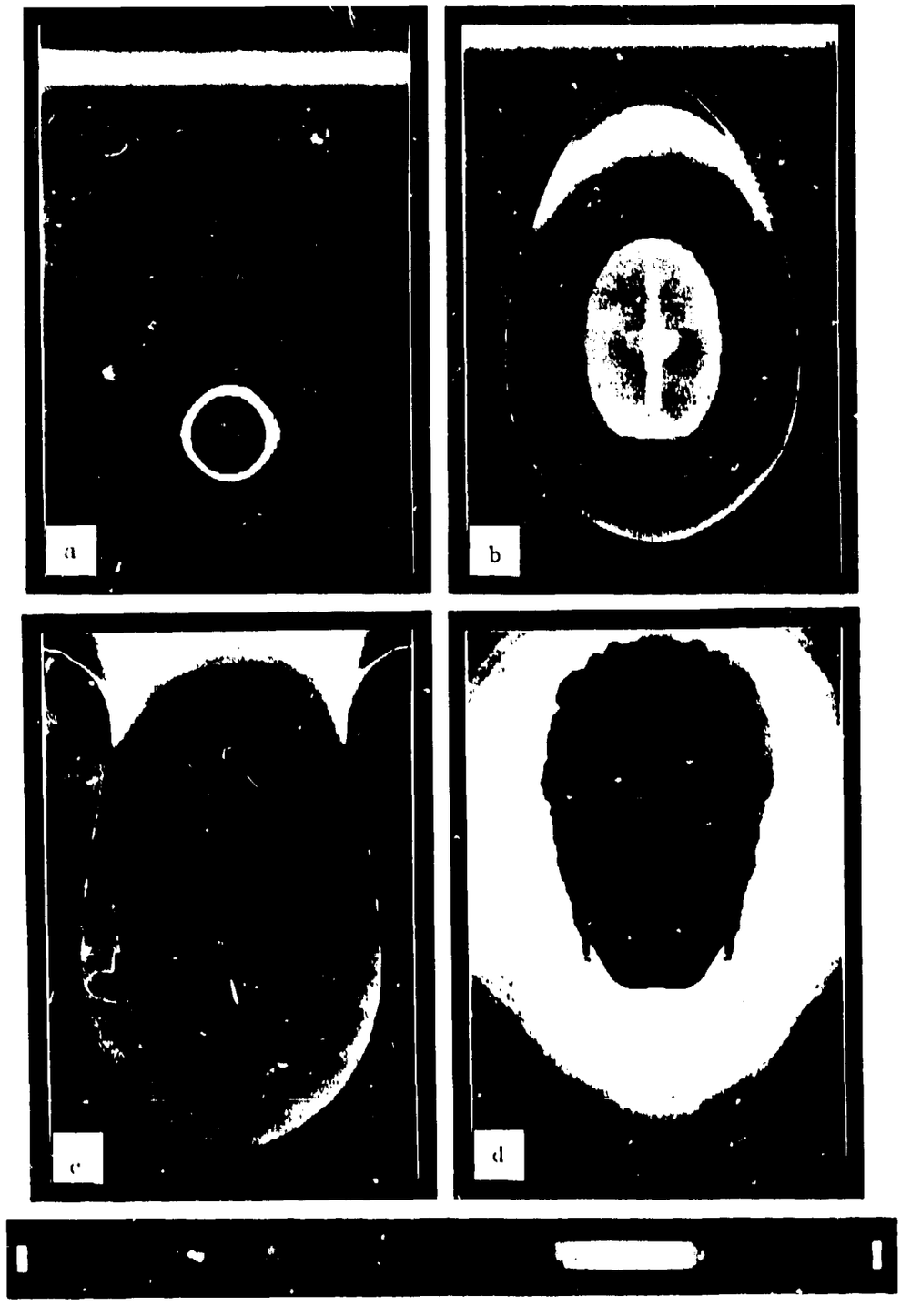

Plate 3

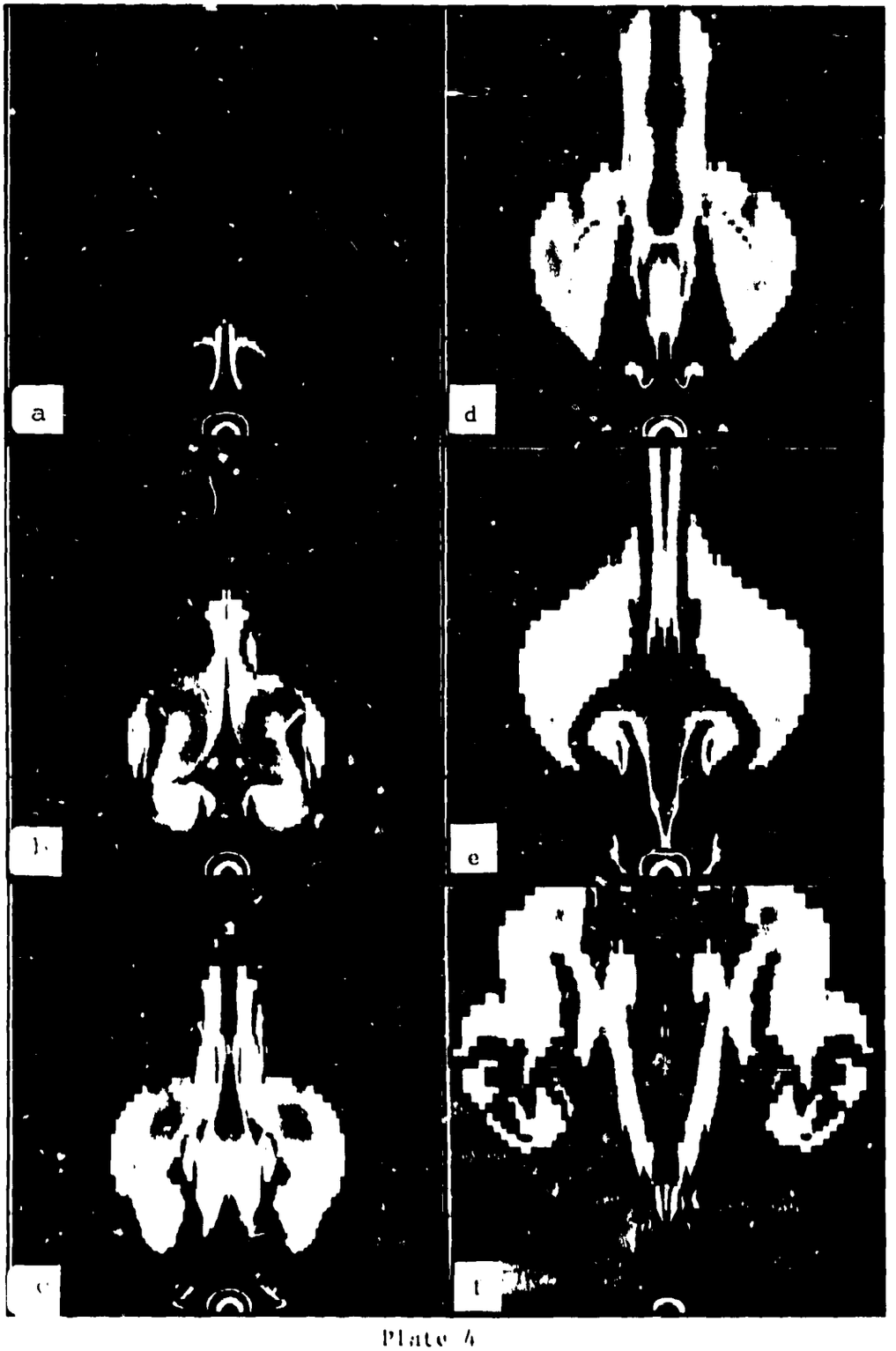

Plate 4

Captions to color plates

Plate 1. The time evolution of an axisymmetric supersonic jet. The plane of the picture contains the symmetry axis of the jet. Gas is continuously introduced from a circular inlet at left, with an internal Mach number of 3, a density 0.1 times the ambient density, and a pressure equal to the ambient pressure. Gas density is represented in 73 shades of color, each color representing an equal logarithmic interval between the maximum and minimum value of the density. The colors are ordered according to the color scale accompanyingPlate 2. Dark blue is minimum and ruddy red is maximum. The jet is divided into a forward moving supersonic beam (green) and a surrounding backward moving cocoon (blue). The boundary between the cocoon and the ambient medium is subject to nonlinear Kelvin-Helmholtz instabilities, which lead to turnover and mixing of the two gases. The computational half-plane comprises 640 equidistant zones in the axial direction and 60 equidistant zones in the radial direction out to 7.5 beam radii, with an additional 15 ratioed zones out to 15 beam radii.

Plate 2. Nonlinear kink instability in a 2-dimensional "slab" jet. Gas is continuously introduced from a slit at the bottom, with an internal Mach number of 3, a density 10 times the ambient density, and a pressure equal to the ambient pressure. The instability is excited by applying a time-varying transverse velocity equal to 5% of the longitudinal velocity, with a frequency corresponding to the fastest-growing unstable mode. Gas density is displayed in color as described in the caption to Plate 1. The instability grows to nonlinear amplitude after convecting a few wavelengths downstream, effectively disrupting the directed bulk flow. Computation performed in Cartesian geometry. The computational plane comprises 300 equidistant zones in the longitudinal direction, 20 equidistant zones across the slab width, and 70 ratioed zones on either side of the midplane extending out to ± 10 slab widths.

Plate 3. Strong point explosion in a plane-stratified exponential atmosphere. Entropy is displayed in color as described in the caption to Plate 1. a) Initial spherical expansion of the high entropy "driver gas" (red) and blastwave-heated ambient gas (yellow). Blastwave radius = 1 scale height. b) Nonspherical evolution of blastwave and hot bubble as it encompasses many scale heights. c) "Breakout" of the blastwave apex as predicted by Kompaneets (1960). d) Bouyant rise of the hot bubble and growth of the Rayleigh-Taylor instability on the leading surface of the bubble. Computation performed in cylindrical geometry assuming axisymmetry, with axis running vertically through the center of each plot. Computational half-plane comprises 360 axial by 120 radial equidistant, square zones.

Plate 4. Time evolution of jet formation via the Blandford-Rees (1974) Twin-Exhaust mechanism. Gas temperature is displayed in color as described in the caption to Plate 1. a) A bubble of hot gas is initially inflated by the central source. b-c) The nozzle forms as the bubble rises due to bouyancy. d) Nozzle constricts leading to inflation of the subsonic cavity surrounding the central source. e-f) A global Rayleigh-Taylor instability introduces dense ambient gas into the newly-formed jet. Computation performed in cylindrical geometry assuming axisymmetry and equatorial symmetry. Computational domain comprises 100 x 100 ratioed zones in the radial and axial directions spanning $0 \le Z \le 10h$, $0 \le R \le 10h$, with a central zone size of $h/100$, where h is the plateau scale height.